

# H4.2

---

## *Transition-edge Sensors*

---

Douglas A. Bennett <sup>1</sup>

---

### H4.2.1 Introduction

Near the end of the twentieth century, there was renewed excitement about the potential applications of a type of superconducting detector known as the transition-edge sensor (TES). In the intervening decades there has been a paradigm shift from the TES as a promising detector being pursued in a handful of laboratories, to these detectors as the central components of important scientific instruments across a broad range of applications. This chapter attempts to give the reader some sense of the broad impact and breadth of uses of TESs by describing the characteristics that have led to their success.

At low temperatures, the suppression of thermal noise enables measurement of the energy and power of photons and particles with great precision. For example, TESs can have resolving powers greater than  $10^3$  at x-ray energies, significantly better than semiconducting detectors. However, the excellent sensitivity of TESs, described in Sec. H4.2.2, is just one reason why TESs have been successfully used in many applications. The other two important factors are the rapid development of robust multiplexing technologies well matched to the properties of TESs (Sec. H4.2.3) and the broad flexibility to detect photons across many orders of magnitude of wavelength (Sec. H4.2.4). For a thorough review of TES physics and design parameters see the reviews by Irwin and Hilton (2005) and Ullom and Bennett (2015).

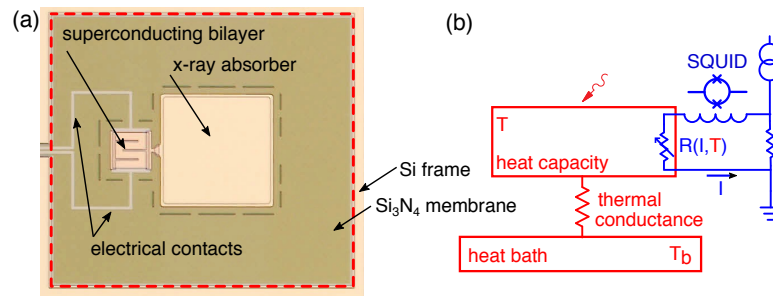
---

### H4.2.2 TES Operational Principles and Sensitivity

A TES consists of a superconducting film connected to small heat capacity that has a weak thermal link to a bath at a fixed temperature, see Fig. H4.2.1. The superconducting film is biased in the superconducting transition so that small changes in temperature correspond to large changes in the resistance of the film. The weak thermal link to a heat bath can be accomplished in a variety of ways depending on the desired thermal conductance ( $G$ ). Wiedemann-Franz thermal conductance becomes exponentially small in superconductors well below the critical temperature ( $T_c$ ), since most of the electrons have formed Cooper pairs and do not scatter. Therefore, superconductors with a transition temperature well above the  $T_c$  of the TES are used to make electrical contact to the TES. In some cases, the weak thermal link between the TES and the bath is due to the bottleneck caused by the decoupling of electrons and phonons at low temperatures (Cabrera et al., 1998; Wei et al., 2008). Often, the TES is fabricated on top of a freestanding micromachined silicon nitride membrane, see Fig. H4.2.1a, and the thermal conductance is dominated by phonon scattering. The thickness of the membrane and the geometry of the device are used to

---

<sup>1</sup>Contribution of the National Institute of Standards and Technology; not subject to copyright in the United States

**FIGURE H4.2.1**

(a) A photograph of an x-ray TES. Inside the dashed line, the silicon has been etched away from underneath the silicon nitride. All the metal inside the dashed line contributes to the heat capacity of the TES. In this case the x-ray absorber is next to the superconducting film and galvanically connected to the TES. Photograph courtesy of Dan Schmidt, NIST.

(b) A schematic representation of the coupled electrical and thermal circuits of a typical TES. The coupling of the electrical and thermal circuits is through the superconducting film, which has a resistance,  $R(I, T)$ , that depends on both the current ( $I$ ) and temperature ( $T$ ).

control the thermal conductance. This mechanism of thermal isolation was pioneered by groups working on bolometers (Downey et al., 1984) and microcalorimeters (Stahle et al., 1996) that predate the use of it in TESs. The thermal conductance can be further reduced by etching holes in the membrane or creating small legs to suspend the membrane. The heat capacity of the TES ( $C$ ) is due to all material isolated by the weak thermal link, including the superconducting film and any additional metal layers.

Modern TESs are almost always operated under voltage bias to take advantage of the stability provided by negative electrothermal feedback (Irwin, 1995). The voltage bias is usually implemented by a shunt resistance, much smaller than the TES resistance, in parallel with the resistance of the TES. The TES is first driven into the normal state where ohmic heating raises the temperature above the  $T_c$  of the superconducting film. The voltage bias is then reduced until the TES is biased in the superconducting transition. Then the ohmic heating of the superconducting film is balanced by the heat removed to the bath through the weak thermal link. The current through the film and the temperature of the TES determine the resistance at this operating point that is some fraction of the normal resistance ( $\%R_n$ ). An increase in the temperature of the device due to absorption of a photon, or some other particle, causes the resistance to increase. Then, due to the stiff voltage bias, an increase in resistance causes a drop in current, and a corresponding drop in the ohmic heating.

The application of TESs can naturally be divided into two categories based on if the TES is used as a microcalorimeter (McCammon, 2005) or a bolometer (Richards, 1994). When used as a microcalorimeter, the TES measures the energy deposited in the heat capacity from a single photon or particle. The temperature rise due to an incoming particle is given by the energy of the particle divided the heat capacity of the microcalorimeter. The response of a TES is then a current pulse, where the height of the pulse and the total area under the pulse are proportional to the incident energy of the particle. If the temperature increase drives the superconducting film above its  $T_c$ , the resistance is driven to  $R_n$  and the device is said to saturate. When driven into saturation, the resolving power of the detector is reduced. Otherwise, the energy resolution is proportional to  $\sqrt{4k_B T^2 C}$ . The full details of the theoretically predicted energy resolution can be found in Irwin and Hilton (2005).

When the TES is used as a bolometer, the incoming electromagnetic radiation is coupled

into the TES where it is converted into heat. In this mode, the change in current from the quiescent state is proportional to the instantaneous power being absorbed averaged over the response time of the TES. Therefore, the response of the TES bolometer is similar to that of a TES calorimeter except that it measures the average power of the signal instead of the energy of a single particle or photon. The thermal conductance of the TES is optimized so that at the optimum bias voltage, the current through the TES goes to zero for the largest anticipated signal. The largest power that a given TES can measure is known as its saturation power. The usual figure of merit for the sensitivity of bolometers is the noise equivalent power (NEP), which is defined as the uncertainty in detected power in a one Hertz bandwidth. The NEP of a TES bolometer is a combination of all the different noise sources in a TES. The details of the relevant noise sources are described in detail by Irwin and Hilton (2005). However, the NEP can generally be improved going to lower temperatures and by reducing the thermal conductance to the bath. For sensitive measurements of astrophysical signals, the NEP of the TES is optimized to be smaller than photon noise of the signal while achieving a sufficient saturation power.

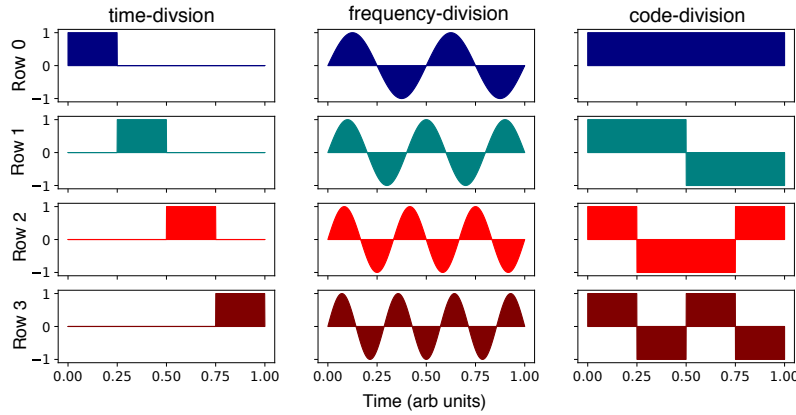
The superconducting quantum interference device (SQUID) amplifier, see Chapter H3.2, is the natural partner to the TES. The low resistance of a TES is easily impedance-matched to SQUID amplifiers. The TES current is easily transformed to a flux in the SQUID, shown schematically in Fig. H4.2.1b. SQUID amplifiers can be optimized to make the readout noise subdominant to the detector noise. Since SQUIDs have low power dissipation and TESs are already operated at temperatures below a kelvin, SQUIDs can be packaged directly with a TES array, for example using bump bonding (Irwin et al., 2004), or integrated directly on the chip with the TESs (Irwin et al., 2012).

---

### H4.2.3 TES Multiplexing

For many of the most compelling applications of TESs, the scientific impact increases with the size of the array. However, as the array size grows, it becomes increasingly difficult to read out every TES in a separate readout channel due to constraints on the physical space and the cooling power available at the coldest stage. Multiplexing the TESs, or reading out multiple TESs by combining their signals in a smaller number readout channels, is necessary for practical instruments. The wide-spread use of arrays of TESs is inextricably linked to the existence and growing maturity of TES multiplexing (Irwin and Hilton, 2005; Ullom and Bennett, 2015). In order to not degrade performance of the TES array, a multiplexing strategy must implement filtering to remove noise outside the useful signal bandwidth and not add in significant noise from the other channels (Irwin, 2002). Multiplexing strategies can be categorized by the orthogonal basis set that is used to encode the signals from the TESs. The three different basis sets that have been implemented in TES multiplexers are time-division, frequency-division, and code-division, shown for four channels in Fig. H4.2.2.

In time-division multiplexing (TDM), signals from different sensors are combined into a common amplifier and separated from the other sensors in time (Chervenak et al., 1999). The switching between the active sensors is accomplished using a SQUID, or group of SQUIDs, as a switch. The sensors are grouped in  $M$  columns and  $N$  rows. For a given column, the first switch is closed coupling the signal from that sensor into the amplifier. After waiting for transients to settle, the signal is averaged for a fixed time and then opened while the next switch is closed. The process is repeated for all the sensors in the column. Each of the  $N$  rows is measured in turn until they have all been measured and the whole process is repeated. The same process occurs simultaneously in all  $M$  columns. A single pair of control

**FIGURE H4.2.2**

Four channel examples of the three most common basis sets for multiplexing TESs; time-division(left), frequency-division (center) and code-division (right). For each basis set, the output gain is plotted as a function of time.

lines can turn on a given row in all the columns. Therefore, an  $M$  column by  $N$  row TDM SQUID multiplexer requires order of  $M + N$  signal lines instead of the  $M \times N$  that would be necessary if each detector had its own readout chain.

The sampling rate for each channel is  $1/(Nt_s)$ , where  $t_s$  is the time the multiplexer dwells on each channel. Noise above the corresponding Nyquist frequency but below the bandwidth of the readout is aliased into the signal band. This aliased noise causes the readout noise to scale as  $\sqrt{N}$ . The signal can be increased above this noise by increasing the strength of the signal coupling into the multiplexer but at the cost of dynamic range. TDM of TESs has reached a high level of maturity and has been demonstrated in a 64 row configuration (Henderson et al., 2016) to readout TES bolometers and in a 40 row configuration for TES microcalorimeters (Durkin et al., 2019).

Frequency-division multiplexing (FDM) uses distinct frequency tones as the orthogonal basis set, shown in Fig. H4.2.2. In megahertz FDM, the modulation is applied to the bias of the TESs and the signals from  $N$  distinct TESs are summed into a single SQUID amplifier (Yoon et al., 2001). Each TES is connected to an inductor and capacitor that with the TES make a resonant filter. All  $N$  filters are connected to a common bias line. The resonant circuit selects a bandwidth around a target carrier frequency and filters out-of-band signals and noise. The number of wires needed to multiplex an array of TESs is reduced by  $N$ . The bandpass filters must be adequately separated in frequency space to prevent crosstalk. Since all the carrier tones are summed together in the SQUID, they must share the SQUID's limited dynamic range. In order to reduce the needed dynamic range, feedback is used to cancel the carriers and signals from the TES (de Haan et al., 2012; den Hartog et al., 2009). The signals are demultiplexed by room temperature electronics before applying the feedback signal. A challenge in megahertz FDM is to minimize stray inductances and other series impedance that can affect the stability of the voltage-bias and cause crosstalk between channels (de Haan et al., 2019). Megahertz FDM has been demonstrated in a 64 row configuration for TES bolometers (Bender et al., 2019) and in a 10 row configuration for TES microcalorimeters (Akamatsu et al., 2018).

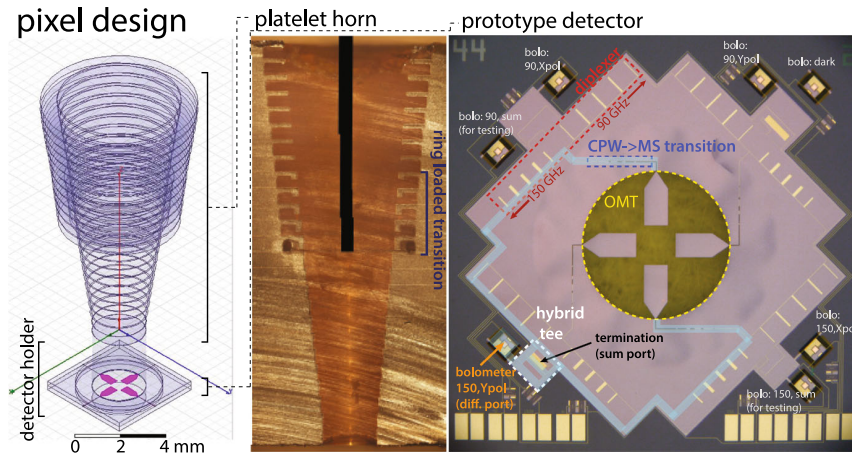
Code-division multiplexing (CDM) uses Walsh codes as the orthogonal modulation functions (Karasik and McGrath, 2001; Irwin et al., 2010). Figure H4.2.2 shows an example of a four channel Walsh code. The signals from all TESs are summed with a polarity pattern that

changes for each column of the Walsh code. A matrix inversion is performed on a sequence of measurements to separate the signals back into signals from individual sensors. CDM has many of the advantages of TDM, but unlike TDM, it does not suffer from the  $\sqrt{N}$  noise penalty and should be suitable for larger multiplexing factors. The polarity switching can be accomplished either by fabricating the Walsh code pattern into the coupling to the SQUIDs ( $\Phi$ -CDM) or by implementing superconducting switches (I-CDM) (Irwin et al., 2010). Both  $\Phi$ -CDM (Stiehl et al., 2012) and I-CDM (Niemack et al., 2010) have been demonstrated at small pixel counts. More recently,  $\Phi$ -CDM has been demonstrated for x-rays TESs in a 32 channel format (Morgan et al., 2016). The combined spectra from 30 of the 32 channels showed a FWHM resolution of 2.77eV at 5.9 keV. CDM has the potential to readout kilopixel arrays of x-ray TES microcalorimeters and could potentially be combined with other multiplexing techniques for larger arrays.

In any multiplexing implementation, the multiplexing factor is limited by available bandwidth. The efficiency of bandwidth utilization is important to achieving a high multiplexing factor (Irwin, 2009). However, more pixels could be multiplexed by going to higher readout bandwidths. The bandwidth of TDM, CDM, and megahertz FDM are all limited to below 10 MHz. The aim of microwave SQUID multiplexing is to significantly increase multiplexing factors by taking advantage of higher bandwidth amplifiers available up in the gigahertz frequency range (Irwin and Lehnert, 2004). It then benefits from the rapid advances in digital to analog converters and analog to digital converters used for software-defined radio and modern radar.

Like megahertz FDM, microwave SQUID multiplexing also utilizes the frequency-division basis set. In microwave SQUID multiplexing, the TES current shifts the resonance frequency of a microwave resonator. By coupling many of microwave resonators at unique frequencies to a common feedline, many TESs can be readout simultaneously with two transmission lines and a pair of lower bandwidth signal lines to modulate the signal. An rf SQUID is used to convert the TES signals into a frequency shift in the resonator (Mates et al., 2008). The rf SQUID is operated below its critical current in the non-dissipative state, where a change of the flux in the SQUID causes a change in the Josephson inductance of the SQUID. The SQUID is coupled to a superconducting resonator such that changes in the inductance of the SQUID shift its resonant frequency. The rf SQUID has its usual periodic response where it is most sensitive to flux changes at a quarter and three quarters of integer flux quanta and insensitive at half integer numbers of a flux quanta. A flux bias to each SQUID would spoil the multiplexing advantage. Instead, flux ramp modulation (Mates et al., 2012) is applied to ramp the flux at frequency  $f_{fr}$  over integer number of flux quanta  $N_{fr}$  causing the signal to be modulated at a frequency  $N_{fr}f_{fr}$ . With flux ramp modulation, the flux at the input of the SQUID is proportional to the phase shift of the modulated signal. Therefore flux ramp modulation effectively linearizes the response of the SQUID multiplexer. It has the additional advantage of modulating the signal up to frequencies above the two-level system noise of the superconducting resonator.

Microwave SQUID multiplexing has been used to multiplex 128 gamma-ray TESs using 2 coaxial cables and a handful of twisted wire pairs (Mates et al., 2017). Microwave SQUID multiplexing has been demonstrated to have sufficiently low noise and crosstalk (Dober et al., 2017) to be suitable for large scale TES instruments measuring the cosmic microwave background (Galitzki et al., 2018). It is also planned to be used in a number of other future instruments including a TES x-ray spectrometer being built for the LCLS-II (Li et al., 2018) and the Lynx X-ray Microcalorimeter on the Lynx satellite (Bennett et al., 2019), currently under study as a potential NASA flagship mission.

**FIGURE H4.2.3**

Left design of a single horn coupled multichroic polarimeter with labels on the major components. Center a photograph of a cross-section of a broad-band ring-loaded corrugated feed horn fabricated by gold plating a stack of etched silicon platelets. Right a photograph of a prototype 90/150 multichroic detector with the major components labeled. For clarity, the path light follows to reach the bolometer corresponding to Y polarization in the 150 GHz band has been highlighted. Reprinted with permission from Datta et al. (2014). Copyright 2014, Springer Nature

#### H4.2.4 Coupling TESs to Signals

TESs have been successfully applied in many measurement applications at vastly different wavelengths. In order to couple to a signal of interest, the signal only needs to be converted into a temperature rise of the heat capacity of the TES. The TES owes its flexibility and broad applicability to the fact that photons, and most other particles, are readily converted into heat. Next, we highlight a few examples of how TESs are optimized to couple to different types of particles and photons at different wavelengths.

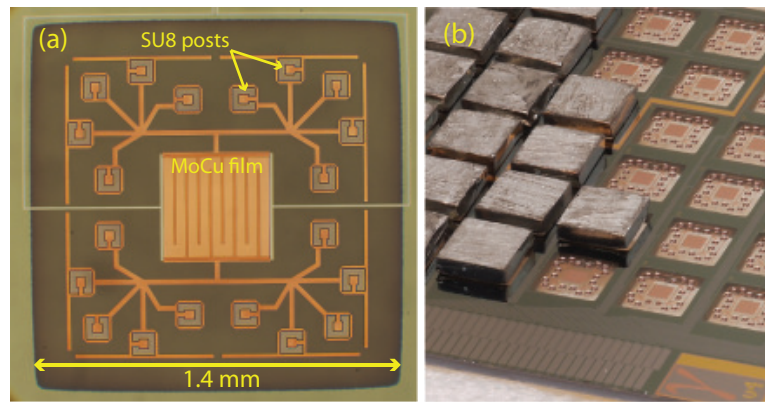
For astronomical instruments at millimeter and submillimeter wavelengths, TESs have become a standard detector technology due to their low noise and ability to scale to large arrays. These qualities are especially apparent for instruments mapping the polarization of the cosmic microwave background (CMB) (Thornton et al., 2016; Bleem et al., 2012). Many TES instruments at these wavelengths are used in a large variety of astronomical observations (Zmuidzinas and Richards, 2004; Mouskops, 2018). Here we describe how one such instrument, ACTPol, uses TESs to observe the CMB at 90 GHz and 150 GHz, see Fig. H4.2.3. First the signal bands at 90 GHz and 150 GHz are collected in dishes that focus the power on to the detector focal plane. The power is coupled into corrugated feed horns made of stacked silicon wafers. Broad-band orthomode transducers (OMTs) are integrated into each feedhorn cavity to couple the power onto the wafer containing the TES. The OMT also separates the power into the orthogonal linear polarizations. Then the 90 and 150 GHz signal bands are separated from each other by on-chip diplexers. Finally, the powers are converted into heat in a termination on the TESs. In Fig. H4.2.3(right), the signal path for the Y polarization of the 150 GHz band is highlighted. It takes four TESs to measure the two frequency bands (90,150) and two polarization at each frequency band (X,Y). However,

seven TESs are used for the test pixel shown in Figure H4.2.3 (right). Besides the four TESs to measure the CMB signals, there are also two TESs for testing purposes and a “dark” TES that is not connected to the OMT and used as a diagnostic.

In far-infrared astronomy, TESs are being utilized in a large variety of observatories for both ground based (Holland et al., 2013) and suborbital astronomy (Harper et al., 2018). More information on TES instruments for far-infrared astronomy can be found in a recent review by Farrah et al. (2019). Metal films with optimized surface impedance can be deposited onto the TES membrane to couple to the far-infrared radiation. TES chips can also be integrated with other structures to provide reflective back-shorts (Jackson et al., 2011; Jhabvala et al., 2014) or absorbers to prevent reflections (Harper et al., 2018). TESs are especially important for potential satellite missions, the SPace Infrared telescope for Cosmology and Astrophysics (SPICA) and the Origins Space Telescope (OST), using actively cooled telescopes ( $\sim 5$  K) to achieve noise equivalent powers dominated by foregrounds. To take full advantage of these platforms for large-area wide-band spectroscopy, NEPs on the order of  $10^{-19}$  W/ $\sqrt{\text{Hz}}$  are necessary (Jackson et al., 2011; Staguhn et al., 2018). Using a Ti TES operating in the hot-electron regime to utilize electron-phonon decoupling to achieve small thermal conductance, Karasik and Cantor (2011) have demonstrated an NEP of  $3 \times 10^{-19}$  W/ $\sqrt{\text{Hz}}$  at 650 GHz measured optically using a black-body source. Researchers at the NASA Jet Propulsion Laboratory (Beyer et al., 2012) and SRON Netherlands Institute for Space Research (Suzuki et al., 2016) have demonstrated electrical NEPs, which do not take into optical coupling loss, of  $1 \times 10^{-19}$  W/ $\sqrt{\text{Hz}}$  in TES bolometers suspended using very low cross-section silicon nitride legs.

At shorter wavelengths, in the optical regime, the photons can be directly absorbed in the superconducting bilayer. The resolution of TESs is sufficient to resolve the number of photons at telecommunication wavelengths (Lita et al., 2008). In order to capture the photons with the highest efficiency, the TES can be incorporated into an optical cavity with antireflection coating appropriate for the wavelength of interest (Rosenberg et al., 2004). To accurately and repeatably align with optical photons inside a cryostat, the TES can be fabricated in a structure that self-aligns with fiber optic cables. The alignment is accomplished by micromachining the silicon wafer that contains the TES into a circular shape that fits inside of a zirconia alignment sleeve that is then attached to the fiber ferrule (Miller et al., 2011). With this packaging the losses of photons coupled in on fibers can be less than 1% (Miller et al., 2011). These properties enable many interesting application for quantum information (Giustina et al., 2013) and quantum cryptography (D. Smith et al., 2012).

Moving to even shorter wavelengths, x-rays TESs take advantage of materials that can stop x-rays with high efficiency while keeping the total heat capacity low. The x-ray absorbers are usually galvanically connected to the TES such that the heat is much more readily moved to the TES than through the weak thermal conductance to the substrate. An x-ray absorbing material can be deposited directly on top the TES membrane, as shown in Fig. H4.2.1, or cantilevered overtop the TES and only connected to superconducting film through metallic posts or stems (Iyomoto et al., 2008). The absorber material and total heat capacity of the TES can be optimized for any x-ray energy from soft x-rays up to hard x-rays. TES have been demonstrated a full-width at half-maximum energy resolution of 0.9 eV at 1.5 keV (Bandler et al., 2013) and 1.58 eV at 5.9 keV (S. Smith et al., 2012). Since the absorbing materials are good at stopping photons, the relative efficiency of an x-ray TES can be very high. However, the small size, on order of 100  $\mu\text{m}$ , required to keep the heat capacity low also results in low absolute efficiencies. However, microfabrication techniques allow the x-ray TESs to be made in large arrays. The ability to achieve excellent resolutions in an energy dispersive detector with good efficiencies are useful in a variety of measurement scenarios; including as instruments at x-ray beam lines (Doriese et al., 2017),

**FIGURE H4.2.4**

(a) A photograph of a TES for gamma-ray spectroscopy. Superconducting leads come in from the left and right sides of the TES. Copper fingers connects the TES to horse-shoe shaped epoxy posts. The posts are attachment points for a bulk tin absorber. The TES is fabricated on a  $\text{Si}_3\text{N}_4$  membrane that appears dark in the photo. (b) A portion of a detector chips where some of the TESs have their bulk absorbers attached. Reprinted with permission from Bennett et al. (2012). Copyright 2012, AIP Publishing LLC.

imaging spectrometers for x-ray satellites (Barret et al., 2018), and for x-ray spectroscopy of hadronic atoms (Okada et al., 2016).

At higher energies, above  $\approx 40$  keV, the relative efficiency becomes very low for materials that can be deposited on to the TES wafer. However, bulk absorbers can be attached to posts fabricated on top of the TES (Zink et al., 2006). A gamma-ray stopped in the bulk absorber material creates heat which must travel through the posts into the TES. The large volume of these bulk absorbers would normally provide too much heat capacity for high resolution spectroscopy. However, if a superconducting absorber is used, it can provide significant stopping power while having low heat capacity. Below its transition temperature the heat capacity falls off quadratically and can be quite small at the usual operating temperature of a TES. TESs of this type have demonstrated FWHM resolutions of 22 eV at 97.43 keV (Bacrania et al., 2009). Once again, the gamma-ray TESs can be fabricated into arrays to increase the overall efficiency (Bennett et al., 2012), see Fig. H4.2.4. The combination of good energy resolution and high efficiency are appealing for applications such as nuclear materials analysis (Hoover et al., 2013).

As a final example, TESs can be used to measure the energy of a nuclear process by incorporating the sample inside the absorber. The sample can either be embedded in a deposited absorber during detector fabrication or encapsulated in a bulk absorber and attached to the TES similar to the gamma-ray TES just described. Assuming no particles escape the absorber, all of the energy of the nuclear decay is converted into heat. This type of device can be used to give isotopic information for trace samples (Lee et al., 2010; Koehler et al., 2013) or can be used to directly measure the mass of the neutrino (Alpert et al., 2015; Croce et al., 2016). For the neutrino mass measurement, an isotope is chosen that has a nuclear decay that gives off a single neutrino with low total energy. The energy of all the decay products is measured except that of the neutrino, which easily escapes the absorber. By measuring the spectrum of many such decays, the rest mass of the neutrino can be inferred from the shape of the spectrum at the endpoint. Experiments are in progress to encapsulate  $\text{Ho}153$  in TESs and could be capable of a direct measurement of the neutrino mass (Nucciotti et al., 2018).

---

#### **H4.2.5 Conclusion**

The TES combines very high sensitivity with the potential for large sensor arrays and broad flexibility to couple to different signals, to meet a large variety of measurement challenges. Besides the examples listed previously, TESs are being implemented in instruments for pigment analysis in the context of art history using particle-induced X-ray emission (Palosaari et al., 2016), for studying chemical reactions with time-resolved x-ray spectroscopy (O’Neil et al., 2017), for the detection of weapons using passive terahertz imagers (Becker et al., 2011), and for searches for dark matter candidates (CDMS II Collaboration et al., 2010). When the voltage biased TES was proposed, it was a novel idea pursued by a small number of researchers who saw its potential to make high sensitivity measurements. Two decades later, this promise is being fulfilled by many groups worldwide, applying TESs to some of the most difficult industrial and scientific measurement problems.

---

## References

---

- Akamatsu, H., Gottardi, L., van der Kuur, J., et al. (2018). Development of frequency domain multiplexing for the x-ray integral field unit (X-IFU). In *Space Telescopes and Instrumentation 2018: Ultraviolet to Gamma Ray*, Volume 10699, pp. 106991N. International Society for Optics and Photonics.
- Alpert, B., Balata, M., Bennett, D., et al. (2015). Holmes. *The European Physical Journal C* 75(3), 112.
- Bacrania, M., Hoover, A., Karpus, P., et al. (2009). Large-area microcalorimeter detectors for ultra-high-resolution x-ray and gamma-ray spectroscopy. *IEEE Transactions on Nuclear Science* 56(4), 2299–2302.
- Bandler, S. R., Adams, J. S., Bailey, C. N., et al. (2013). Advances in small pixel TES-based x-ray microcalorimeter arrays for solar physics and astrophysics. *IEEE Transactions on Applied Superconductivity* 23(3), 2100705.
- Barret, D., Trong, T. L., Den Herder, J.-W., et al. (2018). The ATHENA x-ray integral field unit (X-IFU). In *Space Telescopes and Instrumentation 2018: Ultraviolet to Gamma Ray*, Volume 10699, pp. 106991G. International Society for Optics and Photonics.
- Becker, D., Gentry, C., Ade, P., et al. (2011). High-resolution passive video-rate imaging at 350 GHz. In *Passive Millimeter-Wave Imaging Technology XIV*, Volume 8022, pp. 802206. International Society for Optics and Photonics.
- Bender, A., Anderson, A., Avva, J., et al. (2019). On-sky performance of the SPT-3G frequency-domain multiplexed readout. *arXiv preprint arXiv:1907.10947*.
- Bennett, D. A., Horansky, R. D., Schmidt, D. R., et al. (2012). A high resolution gamma-ray spectrometer based on superconducting microcalorimeters. *Review of Scientific Instruments* 83(9), 093113.
- Bennett, D. A., Mates, J. A., Bandler, S. R., et al. (2019). Microwave SQUID multiplexing for the Lynx x-ray microcalorimeter. *Journal of Astronomical Telescopes, Instruments, and Systems* 5(2), 021007.
- Beyer, A. D., Kenyon, M., Echternach, P., et al. (2012). Development of fast, background-limited transition-edge sensors for the background-limited infrared/sub-mm spectrograph (bliss) for spica. In *Millimeter, Submillimeter, and Far-Infrared Detectors and Instrumentation for Astronomy VI*, Volume 8452, pp. 84520G. International Society for Optics and Photonics.
- Bleem, L., Ade, P., Aird, K., et al. (2012). An overview of the SPTpol experiment. *Journal of Low Temperature Physics* 167(5-6), 859–864.
- Cabrera, B., Clarke, R., Colling, P., et al. (1998). Detection of single infrared, optical, and ultraviolet photons using superconducting transition edge sensors. *Applied Physics Letters* 73(6), 735–737.

- CDMS II Collaboration et al. (2010). Dark matter search results from the CDMS II experiment. *Science* 327(5973), 1619–1621.
- Chervenak, J., Irwin, K. D., Grossman, E. N., et al. (1999). Superconducting multiplexer for arrays of transition edge sensors. *Applied Physics Letters* 74(26), 4043–4045.
- Croce, M. P., Rabin, M. W., Mocko, V., et al. (2016). Development of holmium-163 electron-capture spectroscopy with transition-edge sensors. *Journal of Low Temperature Physics* 184(3-4), 958–968.
- Datta, R., Hubmayr, J., Munson, C., et al. (2014). Horn coupled multichroic polarimeters for the Atacama Cosmology Telescope polarization experiment. *Journal of Low Temperature Physics* 176(5-6), 670–676.
- de Haan, T., Smecher, G., and Dobbs, M. (2012). Improved performance of TES bolometers using digital feedback. In *Millimeter, Submillimeter, and Far-Infrared Detectors and Instrumentation for Astronomy VI*, Volume 8452, pp. 84520E. International Society for Optics and Photonics.
- de Haan, T., Suzuki, A., Boyd, S., et al. (2019). Recent advances in frequency-multiplexed TES readout: Vastly reduced parasitics and an increase in multiplexing factor with subkelvin SQUIDS. *arXiv preprint arXiv:1908.07642*.
- den Hartog, R., Boersma, D., Bruijn, M., et al. (2009). Baseband feedback for frequency-domain-multiplexed readout of TES x-ray detectors. *AIP Conference Proceedings* 1185(1), 261–264.
- Dober, B., Becker, D. T., Bennett, D. A., et al. (2017). Microwave SQUID multiplexer demonstration for cosmic microwave background imagers. *Applied physics letters* 111(24), 243510.
- Doriese, W. B., Abbamonte, P., Alpert, B. K., et al. (2017). A practical superconducting-microcalorimeter x-ray spectrometer for beamline and laboratory science. *Review of Scientific Instruments* 88(5), 053108.
- Downey, P., Jeffries, A., Meyer, S., et al. (1984). Monolithic silicon bolometers. *Applied optics* 23(6), 910–914.
- Durkin, M., Adams, J. S., Bandler, S. R., et al. (2019). Demonstration of Athena X-IFU compatible 40-row time-division-multiplexed readout. *IEEE Transactions on Applied Superconductivity* 29(5), 1–5.
- Farrah, D., Smith, K. E., Ardila, D., et al. (2019). far-infrared instrumentation and technological development for the next decade. *Journal of Astronomical Telescopes, Instruments, and Systems* 5(2), 020901.
- Galitzki, N., Ali, A., Arnold, K. S., et al. (2018). The Simons observatory: instrument overview. In *Millimeter, Submillimeter, and Far-Infrared Detectors and Instrumentation for Astronomy IX*, Volume 10708, pp. 1070804. International Society for Optics and Photonics.
- Giustina, M., Mech, A., Ramelow, S., et al. (2013). Bell violation using entangled photons without the fair-sampling assumption. *Nature* 497(7448), 227.
- Harper, D. A., Runyan, M. C., Dowell, C. D., et al. (2018). HAWC+, the far-infrared camera and polarimeter for SOFIA. *Journal of Astronomical Instrumentation* 7(04), 1840008.

- Henderson, S. W., Stevens, J. R., Amiri, M., et al. (2016). Readout of two-kilopixel transition-edge sensor arrays for Advanced ACTPol. In *Millimeter, Submillimeter, and Far-Infrared Detectors and Instrumentation for Astronomy VIII*, Volume 9914, pp. 99141G. International Society for Optics and Photonics.
- Holland, W., Bintley, D., Chapin, E., et al. (2013). SCUBA-2: the 10 000 pixel bolometer camera on the james clerk maxwell telescope. *Monthly Notices of the Royal Astronomical Society* 430(4), 2513–2533.
- Hoover, A. S., Winkler, R., Rabin, M. W., et al. (2013). Determination of plutonium isotopic content by microcalorimeter gamma-ray spectroscopy. *IEEE Transactions on Nuclear Science* 60(2), 681–688.
- Irwin, K. (1995). An application of electrothermal feedback for high resolution cryogenic particle detection. *Applied Physics Letters* 66(15), 1998–2000.
- Irwin, K., Niemack, M., Beyer, J., et al. (2010). Code-division multiplexing of superconducting transition-edge sensor arrays. *Superconductor Science and Technology* 23(3), 034004.
- Irwin, K. D. (2002). SQUID multiplexers for transition-edge sensors. *Physica C: Superconductivity* 368(1-4), 203–210.
- Irwin, K. D. (2009). Shannon limits for low-temperature detector readout. In *AIP Conference Proceedings*, Volume 1185, pp. 229–236. AIP.
- Irwin, K. D., Audley, M. D., Beall, J. A., et al. (2004). In-focal-plane SQUID multiplexer. *Nuclear Instruments and Methods in Physics Research Section A: Accelerators, Spectrometers, Detectors and Associated Equipment* 520(1-3), 544–547.
- Irwin, K. D., Cho, H.-M., Doriese, W. B., et al. (2012). Advanced code-division multiplexers for superconducting detector arrays. *Journal of Low Temperature Physics* 167(5-6), 588–594.
- Irwin, K. D. and Hilton, G. C. (2005). Transition-edge sensors. In C. Enss (Ed.), *Cryogenic particle detection*, pp. 63–150. Springer.
- Irwin, K. D. and Lehnert, K. W. (2004). Microwave SQUID multiplexer. *Applied physics letters* 85(11), 2107–2109.
- Iyomoto, N., Bandler, S., Brekosky, R., et al. (2008). Close-packed arrays of transition-edge x-ray microcalorimeters with high spectral resolution at 5.9 keV. *Applied Physics Letters* 92(1), 013508.
- Jackson, B., De Korte, P., Van der Kuur, J., et al. (2011). The spica-safari detector system: Tes detector arrays with frequency-division multiplexed squid readout. *IEEE Transactions on Terahertz Science and Technology* 2(1), 12–21.
- Jhabvala, C. A., Benford, D. J., Brekosky, R. P., et al. (2014). Kilopixel backshort-under-grid arrays for the primordial inflation polarization explorer. In *Millimeter, Submillimeter, and Far-Infrared Detectors and Instrumentation for Astronomy VII*, Volume 9153, pp. 91533C. International Society for Optics and Photonics.
- Karasik, B. and McGrath, W. (2001, February). Novel multiplexing technique for detector and mixer arrays 12th int. In *Symp. on Space Terahertz Technology*, San Diego, California, USA.

- Karasik, B. S. and Cantor, R. (2011). Demonstration of high optical sensitivity in far-infrared hot-electron bolometer. *Applied Physics Letters* 98(19), 193503.
- Koehler, K., Bennett, D., Bond, E., et al. (2013).  $q$  spectroscopy with superconducting sensor microcalorimeters. *IEEE Transactions on Nuclear Science* 60(2), 624–629.
- Lee, S.-J., Lee, M. K., Jang, Y. S., et al. (2010). Cryogenic measurement of alpha decay in a  $4\pi$  absorber. *Journal of Physics G: Nuclear and Particle Physics* 37(5), 055103.
- Li, D., Alpert, B., Becker, D., et al. (2018). TES x-ray spectrometer at SLAC LCLS-II. *Journal of Low Temperature Physics* 193(5-6), 1287–1297.
- Lita, A. E., Miller, A. J., and Nam, S. W. (2008). Counting near-infrared single-photons with 95% efficiency. *Optics express* 16(5), 3032–3040.
- Mates, J., Becker, D. T., Bennett, D. A., et al. (2017). Simultaneous readout of 128 x-ray and gamma-ray transition-edge microcalorimeters using microwave SQUID multiplexing. *Applied Physics Letters* 111(6), 062601.
- Mates, J., Hilton, G. C., Irwin, K. D., et al. (2008). Demonstration of a multiplexer of dissipationless superconducting quantum interference devices. *Applied Physics Letters* 92(2), 023514.
- Mates, J., Irwin, K., Vale, L., et al. (2012). Flux-ramp modulation for SQUID multiplexing. *Journal of Low Temperature Physics* 167(5-6), 707–712.
- Mauskopf, P. (2018). Transition edge sensors and kinetic inductance detectors in astronomical instruments. *Publications of the Astronomical Society of the Pacific* 130(990), 082001.
- McCammon, D. (2005). Thermal equilibrium calorimeters—an introduction. In C. Enss (Ed.), *Cryogenic particle detection*, pp. 1–34. Springer.
- Miller, A. J., Lita, A. E., Calkins, B., et al. (2011). Compact cryogenic self-aligning fiber-to-detector coupling with losses below one percent. *Optics express* 19(10), 9102–9110.
- Morgan, K. M., Alpert, B. K., Bennett, D. A., et al. (2016). Code-division-multiplexed readout of large arrays of TES microcalorimeters. *Applied Physics Letters* 109(11), 112604.
- Niemack, M. D., Beyer, J., Cho, H., et al. (2010). Code-division SQUID multiplexing. *Applied Physics Letters* 96(16), 163509.
- Nucciotti, A., Alpert, B., Balata, M., et al. (2018). Status of the HOLMES experiment to directly measure the neutrino mass. *Journal of Low Temperature Physics* 193(5-6), 1137–1145.
- Okada, S., Bennett, D., Curceanu, C., et al. (2016). First application of superconducting transition-edge sensor microcalorimeters to hadronic atom x-ray spectroscopy. *Progress of Theoretical and Experimental Physics* 2016(9).
- O’Neil, G. C., Miaja-Avila, L., Joe, Y. I., et al. (2017). Ultrafast time-resolved x-ray absorption spectroscopy of ferrioxalate photolysis with a laser plasma x-ray source and microcalorimeter array. *The journal of physical chemistry letters* 8(5), 1099–1104.
- Palosaari, M., Käyhkö, M., Kinnunen, K., et al. (2016). Broadband ultrahigh-resolution spectroscopy of particle-induced x rays: extending the limits of nondestructive analysis. *Physical Review Applied* 6(2), 024002.

- Richards, P. (1994). Bolometers for infrared and millimeter waves. *Journal of Applied Physics* 76(1), 1–24.
- Rosenberg, D., Nam, S., Miller, A., et al. (2004). Near-unity absorption of near-infrared light in tungsten films. *Nuclear Instruments and Methods in Physics Research Section A: Accelerators, Spectrometers, Detectors and Associated Equipment* 520(1-3), 537–540.
- Smith, D., Gillett, G., De Almeida, M. P., et al. (2012). Conclusive quantum steering with superconducting transition-edge sensors. *Nature communications* 3, 625.
- Smith, S., Adams, J., Bailey, C., et al. (2012). Small pitch transition-edge sensors with broadband high spectral resolution for solar physics. *Journal of Low Temperature Physics* 167(3-4), 168–175.
- Staguhn, J., Amatucci, E., Armus, L., et al. (2018). Origins space telescope: the far infrared imager and polarimeter fip. In *Space Telescopes and Instrumentation 2018: Optical, Infrared, and Millimeter Wave*, Volume 10698, pp. 106981A. International Society for Optics and Photonics.
- Stahle, C., Kelley, R., McCammon, D., et al. (1996). Microcalorimeter arrays for high resolution soft x-ray spectroscopy. *Nuclear Instruments and Methods in Physics Research Section A: Accelerators, Spectrometers, Detectors and Associated Equipment* 370(1), 173–176.
- Stiehl, G., Doriese, W. B., Fowler, J., et al. (2012). Code-division multiplexing for x-ray microcalorimeters. *Applied Physics Letters* 100(7), 072601.
- Suzuki, T., Khosropanah, P., Ridder, M., et al. (2016). Development of ultra-low-noise tes bolometer arrays. *Journal of Low Temperature Physics* 184(1-2), 52–59.
- Thornton, R., Ade, P., Aiola, S., et al. (2016). The Atacama Cosmology Telescope: The polarization-sensitive ACTPol instrument. *The Astrophysical Journal Supplement Series* 227(2), 21.
- Ullom, J. N. and Bennett, D. A. (2015). Review of superconducting transition-edge sensors for x-ray and gamma-ray spectroscopy. *Superconductor Science and Technology* 28(8), 084003.
- Wei, J., Olaya, D., Karasik, B. S., et al. (2008). Ultrasensitive hot-electron nanobolometers for terahertz astrophysics. *Nature nanotechnology* 3(8), 496.
- Yoon, J., Clarke, J., Gildemeister, J., et al. (2001). Single superconducting quantum interference device multiplexer for arrays of low-temperature sensors. *Applied Physics Letters* 78(3), 371–373.
- Zink, B., Ullom, J., Beall, J., et al. (2006). Array-compatible transition-edge sensor microcalorimeter  $\gamma$ -ray detector with 42 eV energy resolution at 103 keV. *Applied Physics Letters* 89(12), 124101.
- Zmuidzinas, J. and Richards, P. L. (2004). Superconducting detectors and mixers for millimeter and submillimeter astrophysics. *Proceedings of the IEEE* 92(10), 1597–1616.